Fabrication of vertical orthorhombic/hexagonal tungsten oxide phase junction with high photocatalytic performance

Yesheng Li [a], Zilong Tang [a,*], Junying Zhang [b,*], Zhongtai Zhang [a]

[a] State Key Laboratory of New Ceramics and Fine Processing, School of Materials Science and Engineering, Tsinghua University, Beijing 100084, China
[b] Key Laboratory of Micro-Nano Measurement, Manipulation and Physics (Ministry of Education), Department of Physics, Beihang University, Beijing 100191, China

ABSTRACT

The common one dimensional (1D) core-shell phase junction usually cannot fully utilize the separated charges because one phase is encapsulated inside, which leads to the incomplete release of the electrons or holes. Here, a unique vertical 1D/1D tungsten oxide phase junction constructed by orthorhombic $WO_3 \cdot 0.33H_2O$ (o-$WO_3 \cdot 0.33H_2O$) nanorods and hexagonal WO_3 (h-WO_3) nanowires in the sunflower-like structure was fabricated via a facile one-step hydrothermal method. The nanorods and the nanowires vertically intersect at the endpoint to construct the vertical 1D/1D phase junction with another end exposed outside. This structure ensures that both two phases can contact the pollutants, so as to fully release the holes and electrons that accumulate on the o-$WO_3 \cdot 0.33H_2O$ and h-WO_3 phase, respectively. Furthermore, the two phases are both single crystals, substantially decreasing the impediments of defects to the transport of the photogenerated charges. This novel hierarchical structure with vertical 1D o-$WO_3 \cdot 0.33H_2O$/h-WO_3 phase junction can significantly improve the utilization efficiency of the separated photogenerated charges and thus effectively enhance the photocatalytic performance.

© 2017 Elsevier B.V. All rights reserved.

1. Introduction

Semiconductor photocatalysts have been intensively investigated in the last decades as it is potential for the applications of environmental remediation and clean energy production [1–8]. To achieve this purpose, the key lies in developing proper photocatalysts that can harvest solar light and efficiently separate and transfer photogenerated charges. Various kinds of strategies have been proposed to improve separation and transfer efficiency of the photogenerated charges, among which fabrication of phase junctions is an effective approach [9–12]. The phase junctions in polymorph semiconductors, such as the anatase/rutile phase junction in TiO_2 [2,13–20] and α/β phase junction in Ga_2O_3 [21–25] have been widely investigated. This kind of phase junction constructed by the different phases of the same semiconductor has attracted much attention due to its simplicity, controllability and great photocatalytic activity [26,13].

Tungsten oxide with a band gap of 2.5–2.8 eV is an attractive visible-light-sensitive photocatalyst in organic compounds decomposition, water splitting, and CO_2 photoreduction [26–28]. It is also a kind of polymorph semiconductor which has many crystal phases including tetragonal, orthorhombic, monoclinic, hexagonal, triclinic and especially abundant hydrates (such as $WO_3 \cdot 2H_2O$, $WO_3 \cdot H_2O$, $WO_3 \cdot 0.33H_2O$ and so on). It greatly facilitates the construction of phase junction between different phases of tungsten oxides. Constructing phase junction should be useful for improving the charges separation efficiency of tungsten oxide. However, the photocatalytic activity dependence on the phase junction of tungsten oxides is still preliminarily investigated [6,26,29,30].

Since one-dimensional (1D) nanostructure-based phase junction takes the advantages of 1D nanostructure in shortening the electron diffusion length and enhancing the light absorption [31,32], fabricating 1D tungsten oxide phase junction should be a desirable strategy. The 1D phase junction was commonly constructed by one phase encapsulating the 1D phase to form the 1D core-shell structure [2,17,18,20,32–34]. The 1D core-shell phase junction could improve charges separation and transfer efficiency but it can't fully use the separated charges, because only one phase (the shell) could fully contact the reactants. For examples, the band structures of two phases favor the localization of the photogenerated electrons in the shell and the holes in the core. The holes couldn't be released completely [34] and thus were unable to play the full to react with the pollutants, which is not good for the utilization of the separated charges. There remains challenge of

* Corresponding authors.
E-mail addresses: tzl@tsinghua.edu.cn (Z. Tang), zjy@buaa.edu.cn (J. Zhang).
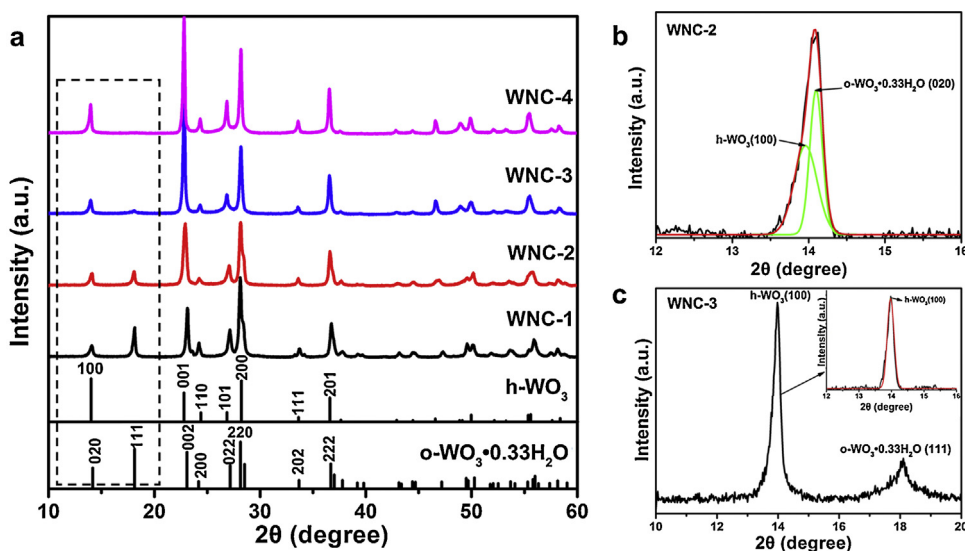
Fig. 1. (a) XRD patterns of the tungsten oxides prepared with different amount of NaCl; (b) XRD pattern fitting analysis of WNC-2; (c) the enlarged picture of WNC-3 at the range of 10–20° and the corresponding XRD pattern fitting analysis (the inset).

fabricating the phase junction that could fully utilize the separated charges.

Herein, a novel vertical 1D/1D tungsten oxide phase junction composed of orthogonal orthorhombic $WO_3 \cdot 0.33H_2O$ (o-$WO_3 \cdot 0.33H_2O$) nanorods and hexagonal WO_3 (h-WO_3) nanowires in the sunflower-like hierarchical structure was synthesized by a simple one-step hydrothermal method. In this structure, the o-$WO_3 \cdot 0.33H_2O$ nanorod and h-WO_3 nanowire substantially vertically intersect at the endpoint to construct the vertical 1D/1D phase junction, while another ends of the nanowire and nanorod are exposed. This structure ensures the spatial separation of the photo-generated electrons and holes, and both the two phases can contact the pollutants and release the separated charges. As a result, the phase junction exhibits superior photocatalytic activities in comparison with the component phases. The photocurrents and electrochemical impedance spectra confirm the high charge separation efficiency of the phase junction.

2. Experimental

All chemicals were purchased from the Sinopharm Chemical Reagent Co., Ltd. and were of analytical reagent grade and used

without further purification. All the aqueous solutions were prepared using deionized water.

### 2.1. Synthesis of the sunflower-like tungsten oxide

A facile one-step hydrothermal method was used to synthesize the sunflower-like tungsten oxide. Typically, 1.25 g H_2WO_4 was added into 25 mL H_2O_2, stirred at 90 °C for 1.5 h before converting into a transparent sol. The resulting clear sol was diluted to 60 mL using deionized water, and then 42 mL of the sol were taken out and diluted to 224 mL using deionized water. After stirring for another 20 min, 30 mL of the precursor solution was transferred into a 50 mL Teflon-lined autoclave followed by adding a certain amount of NaCl. Finally, the autoclave was sealed and maintained at 180 °C for 4 h. The as-synthesized precipitate was washed with deionized water for three times and ethanol for two times, and then dried in vacuum at 80 °C for 5 h. The samples prepared by adding different amount of NaCl were labelled as WNC-1 (0 g NaCl), WNC-2 (0.1 g NaCl), WNC-3 (0.2 g NaCl) and WNC-4 (0.4 g NaCl).

### 2.2. Photo-deposition of Pt or MnO_X on the sunflower-like tungsten oxide

Typically, 1.6 mL 2 mg L^{-1} $H_2PtCl_6 \cdot 6H_2O$ solution and 2 mL CH_3OH were added in the 38 mL WNC-2 suspension which contains 20 mg WNC-2 powder. Then, the suspension was irradiated under 300 W Xenon lamp for 1 h. The products were isolated by centrifugation and washed with deionized water for several times. Similarly, the photo-oxidization of MnO_x was performed with $MnSO_4 \cdot H_2O$ as precursor and $NaIO_3$ as electron acceptor.

2.3. Measurements of photocatalytic and photoelectrochemical properties

The photocatalytic properties of the samples were evaluated by measuring the concentration of rhodamine B (RhB), methyl orange (MO) and colorless phenol in aqueous solution after irradiation with simulated solar light produced by a 300 W Xenon lamp. Typically, 20 mg sample was dispersed in 40 mL dye aqueous solution (15 mg L^{-1}). Prior to irradiation, the suspension was stirred overnight to ensure the equilibrium of dye adsorption on the surfaces of the sample. The dye concentration was measured by UV–vis spec-
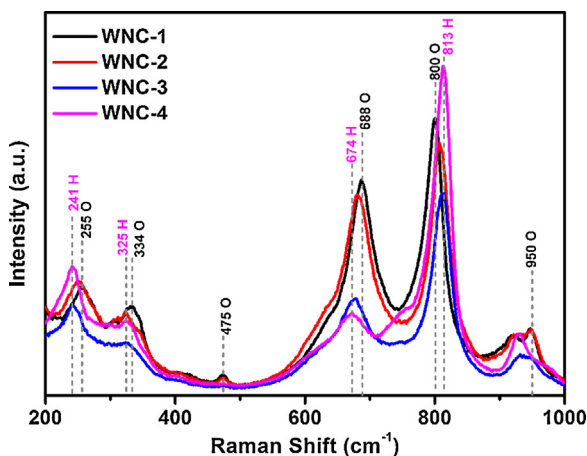
Fig. 2. Raman spectra of the tungsten oxides prepared with different amount of NaCl (O: Orthorhombic $WO_3 \cdot 0.33H_2O$, H: Hexagonal WO_3).
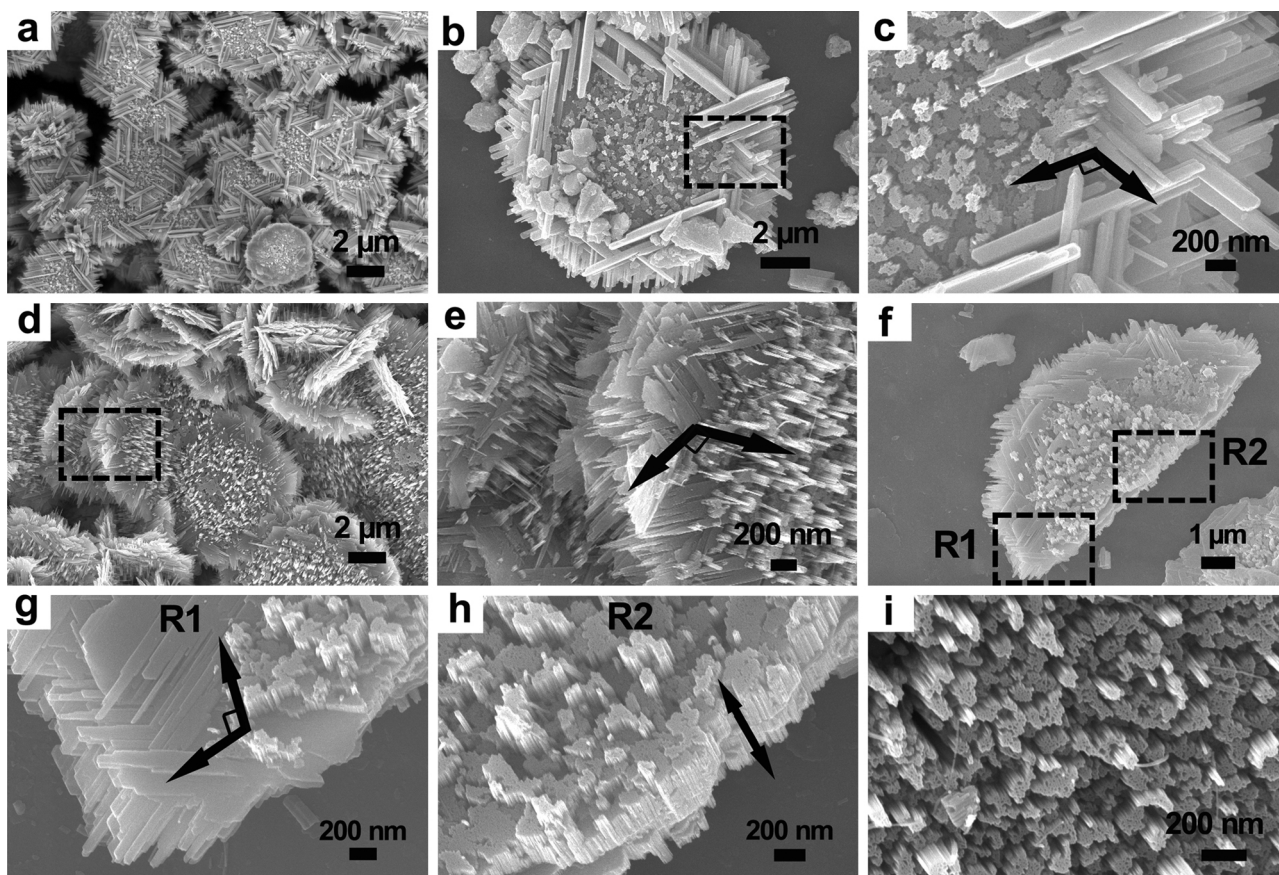
Fig. 3. SEM images of (a–c) WNC-2 with single sunflower-like structure and the corresponding enlarged picture of the rectangular region; (d and e) WNC-3 and the corresponding enlarged picture of the rectangular region; (f–h) a fractured sunflower-like structure (WNC-3) with the corresponding enlarged pictures of the rectangular region 1(R1) and region 2 (R2); (the arrows in Fig. c, e, g and h illustrate the vertical relation of the nanorods and nanowires); (i) the enlarged image of the center region of the sunflower-like tungsten oxide (WNC-2, WNC-3 and WNC-4 have similar morphology in this region).

troscopy. The photodegadation of phenol (10 mg/L) was conducted in a similar procedure to the dye. The concentration of phenol was determined by the chromatographic experiments performed using an HPLC-UV/Vis system with an ultraviolet absorbance detector (K2501) operated at 270 nm and a Venusil XBP-C$_{18}$ (Agela Technologies Inc.) column.

The photocurrents and electrochemical impedance spectra (EIS) were measured on an electrochemical workstation (CHI-660E, China) and carried out in a three-electrode system with a working electrode, a platinum wire as counter electrode and a standard calomel electrode (SCE) as reference electrode. 0.1 M Na$_2$SO$_4$ was used as the electrolyte solution. The photocurrent responses of the photocatalysts were measured at 0.0 V (vs. SCE). The EIS data were carried out at frequencies from 100 mHz to 100 kHz with a magnitude of 5 mV at open-circuit potential. The working electrodes were prepared by a dip-coating method: 10 mg photocatalyst was suspended in 1 mL 1-methyl-2-pyrrolidinone (NMP) to make a slurry, and the slurry was then dip-coated onto a 2 × 3.5 cm fluorine-tin oxide (FTO) glass. The as-prepared electrodes were dried at 80 °C for 10 h in air before measurement.

2.4. Characterization of materials

The X-ray diffraction patterns were obtained on a Rigaku D/max-V2500 (Cu Kα radiation). High-resolution Raman spectroscopy (HR800, Horiba Jobin Yvon, France) were used to collect the Raman spectra. The morphology and microstructure were studied by scanning electron microscopy (SEM, Zeiss, Germany) and transmission electron microscopy (TEM, JEOL-2100F, Japan). The X-ray pho-

toelectron spectroscopy (XPS) measurements were determined on an Escalab 250Xi instrument (Thermo Fisher Scientific, USA). UV–vis spectrophotometer (U-3010, Hitachi, Japan) was used to record UV/Vis absorption spectra. The surface areas of the samples were measured by the Brunauer-Emmett-Teller (BET) method using nitrogen adsorption-desorption isotherms at 77 K with a Contador QuadraSorb SI-MP instrument. The Mott-Schottky plots were measured on an electrochemical workstation (CHI-660E, China) and carried out in a three-electrode system (counter electrode: Pt; reference electrode: standard calomel electrode (SCE); electrolyte: 0.1 M Na$_2$SO$_4$, frequency: 1000 Hz). The photoluminescence (PL) measurements are taken at room temperature using a xenon lamp (Xe900) with an excitation wavelength of 350 nm. Electron spin resonance spectroscopy (ESR) measurements were performed at room temperature with a JEOL FA200 ESR spectrometer under simulated solar light.

3. Results and discussion

3.1. Structure and morphology

The XRD patterns of tungsten oxides prepared using different amount of NaCl were presented in Fig. 1. The (111) diffraction peak at about 18.1° is the characteristic peak of orthorhombic WO$_3$·0.33H$_2$O (o-WO$_3$·0.33H$_2$O), because there is no peak in this position for hexagonal WO$_3$ (h-WO$_3$). The peaks of WNC-1 can be well indexed to o-WO$_3$·0.33H$_2$O (JCPDS no. 72-0199) when no NaCl was added (Fig. 1a). While as the amount of NaCl was increased to 0.4 g, WNC-4 yields a pure h-WO$_3$ phase, with the XRD pat-
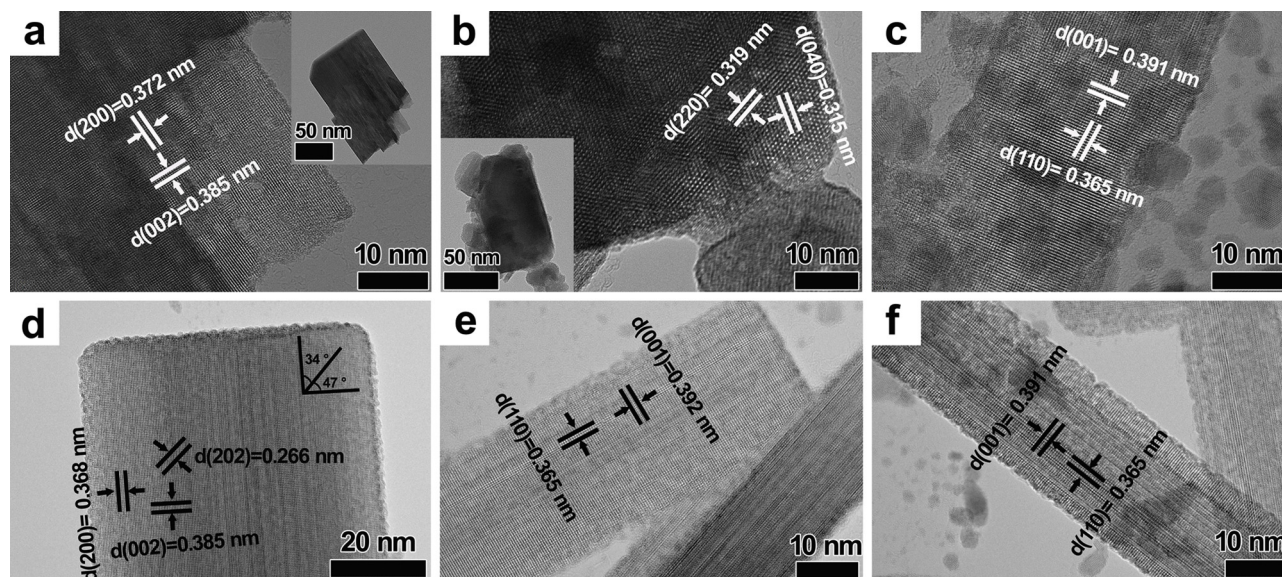
Fig. 4. HRTEM images of (a) nanoplate in WNC-1, (b and c) nanorod and nanowire in WNC-2, (d and e) nanorod and nanowire in WNC-3 and (f) nanowire in WNC-4. (The TEM samples were prepared by sonicating for about 20 min for better observing the nanorods and nanowires.).

tern corresponding to JCPDS no. 75-2187 (Fig. 1a). It seems that WNC-2 can be attributed to the o-WO$_3$·0.33H$_2$O and WNC-3 can be assigned to the h-WO$_3$, as shown in Fig. 1a. However, the peak intensities of WNC-2 at about 14.0 and 18.1° and their intensity ratio are obviously different from those of WNC-1. There is a small peak at 18.1° in WNC-3 which would not appear in the h-WO$_3$. In order to gain insight into the detailed phase information, a numerical deconvolution technique was used. The major phase of WNC-2 is o-WO$_3$·0.33H$_2$O, since it has the obvious peak of (111). But after deconvolution, the peak at about 14.0° can be separated into two peaks belonging to h-WO$_3$ (100) and o-WO$_3$·0.33H$_2$O (020), respectively, as shown in Fig. 1b, suggesting that there exists h-WO$_3$ phase in WNC-2. Similarly, from the enlarged XRD pattern (at range of 10–20°) in Fig. 1c, the o-WO$_3$·0.33H$_2$O (111) peak can be clearly observed and only one peak can be separated in the range of 12–16°(the inset), indicating that WNC-3 not only has h-WO$_3$ but also has a small part of o-WO$_3$·0.33H$_2$O. In summary, WNC-1 and WNC-4 belong to pure o-WO$_3$·0.33H$_2$O and h-WO$_3$, respectively, WNC-2 contains the major phase of o-WO$_3$·0.33H$_2$O and a part of h-WO$_3$, and h-WO$_3$ is the main phase in WNC-3.

The further phase information of the samples was investigated using Raman spectroscopy. The peaks centered at about 255, 334, 472, 688, 800, and 950 cm^{-1} in WNC-1, are assigned to the o-WO$_3$·0.33H$_2$O, as shown in Fig. 2. The peaks at 255 and 334 cm^{-1} are assigned to the W—O—W bending vibration of the bridging oxygen [δ (W—O—W)]. The peaks at around 688 and 800 cm^{-1} are attributed to the stretching vibration of O—W—O [ν (O—W—O)] [35]. The peaks at around 472 and 950 cm^{-1} are assigned to the stretching mode of W—OH$_2$ and the terminal W=O bond, respectively, which are typical peaks for tungsten oxide hydrates [36]. The peaks of h-WO$_3$ centered at about 241, 325, 674, and 813 cm^{-1} are found in WNC-4. The peaks at 241 and 325 cm^{-1} are assigned to δ (W—O—W) and the peaks at around 674 and 813 cm^{-1} are attributed to ν (O—W—O). As for WNC-2, the peak at 800 cm^{-1} red shifts to 808 cm^{-1} and all the other peaks are blue shifted compared with WNC-1 (Fig. 2). The Raman peaks in WNC-3 are similar to those in WNC-4, except that the peak shifts from 674 to 679 cm^{-1} and a peak at 950 cm^{-1} is observed, as shown in Fig. 2. The shifts of Raman peaks in WNC-2 and WNC-3 compared with WNC-1 and WNC-4, in turn confirm the analysis of XRD patterns, i.e. both WNC-2 and WNC-3 have two phases.

The morphology variations of the as-prepared samples are shown in Figs. 3 and S1 . It shows that the sample appears with a ball-flower-like structure assembled with numerous rectangular nanoplates (about 100 nm thick) when no NaCl was used (Fig. S1a and b), while as the NaCl was added in the hydrothermal solution, the samples WNC-2, WNC-3 and WNC-4 all show the sunflower-like shape (Figs. 3 and S1c). The morphologies in the center region of the sunflower-like structures are similar among WNC-2, WNC-3 and WNC-4, as shown in Fig. 3i, all exhibiting nanowire bundle arrays. The area of the nanowire bundle arrays enlarges as the amount of NaCl increases, i.e. WNC-4> WNC-3> WNC-2. However, the outer regions of the sunflower-like structures are different among these three samples. WNC-2 is assembled with nanorods in the outer region (Fig. 3a–c), while the thinner nanorods are linked each other into flake-like shape in the edge of WNC-3 (Fig. 3d–g) and the edge of the WNC-4 is smooth without nanorods (Fig. S1d). Moreover, from the enlarged pictures of the corresponding rectangular region (Fig. 3c and e), it is revealed that the inner nanowires and outer nanorods are substantially vertically intersect in WNC-2 and WNC-3. Meanwhile, a fractured sunflower-like structure was further investigated to confirm the vertical relation of the nanorods and nanowires, as shown in Fig. 3f–h. Above all, the WNC-1 has no nanowire bundles but thick nanoplates and the WNC-4 is completely assembled with nanowire bundles; the WNC-2 and WNC-3 contain orthogonal nanorods and nanowire bundles. The XRD patterns show that the WNC-1 is pure o-WO$_3$·0.33H$_2$O, WNC-4 is pure h-WO$_3$ and WNC-2 and WNC-3 are composed of two phases, suggesting that the nanorods and nanowires may correspond to different crystal phases.

To further analyze the morphology and the crystal phase of the samples, TEM images of the samples were recorded. WNC-2 and WNC-3 containing two kinds of building block-the nanorods and the nanowires-can be confirmed by the TEM images, as shown in Fig. S2. In order to study the structure of the nanorod and nanowire, the HRTEM images were taken and shown in Fig. 4. The spacing of the lattice fringes of the nanoplate in WNC-1 are found to be 0.385 and 0.372 nm, which can be well indexed as (002) and (200) planes of the o-WO$_3$·0.33H$_2$O, as shown in Fig. 4a. WNC-2 contains two kinds of building block: the spacing of the lattice fringes of the thick nanorod are 0.319 and 0.315 nm corresponding to (220) and (040) planes of the o-WO$_3$·0.33H$_2$O (Fig. 4b), and the
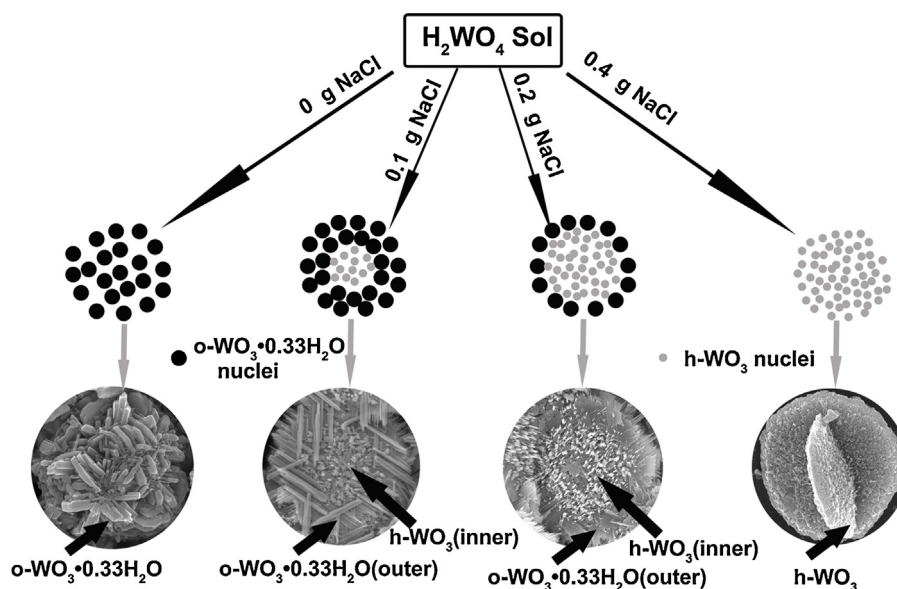
Fig. 5. Illustration of the morphology and crystal phase tuning of tungsten oxide by adjusting the amount of NaCl.

nanowire with a width at about 20 nm has the spacing of the lattice fringes of 0.391 and 0.365 nm belonging to h-WO_3 (Fig. 4c). Similarly, the nanorod in WNC-3 with the spacing of the lattice fringes about 0.385, 0.368 and 0.266 nm are assigned to o-WO_3·0.33H_2O and the nanowire belongs to h-WO_3 (Fig. 4d and e). Moreover, the nanowire in WNC-4 belonging to h-WO_3 shows similar value of the spacing of the lattice fringes to those of the nanowire in WNC-2 and WNC-3. The well-fined lattice fringes demonstrate that both the nanorod and nanowire are single crystal. The results of XRD patterns, Raman spectra and HRTEM images clearly demonstrate that the sunflower-like WNC-2 and WNC-3 are assembled with both o-WO_3·0.33H_2O and h-WO_3, and the thick nanorods in the outer region of the sunflower-like structure belong to o-WO_3·0.33H_2O and the thin nanowires in the centre region are h-WO_3. Therefore, it can infer that the phase junction constructed by nanorod-like o-WO_3·0.33H_2O and nanowire-like h-WO_3 should exist in sunflower-like WNC-2 and WNC-3.

As mentioned above, the addition of NaCl would result in the production of sunflower-like tungsten oxide. And the amount of NaCl is very important for the formation of sunflower-like o-WO_3·0.33H_2O/h-WO_3 phase junction. The relationship between the amount of NaCl and the morphology and crystal phase of the tungsten oxide is illustrated in Fig. 5. Many references reported that NaCl could be the capping agent that leads to the formation of 1D tungsten oxide nanorods or nanowires [37,38]. NaCl could selectively adsorb onto the crystal planes parallel to the c-axes of tungsten oxide crystal nuclei. Then the growth of those crystal planes would be impeded, while the crystal plane perpendicular to c-axes would grow faster, thus leading to the preferential growth along c-axis [37]. In some cases, 1D nanorod could also be synthesized by using Na_2WO and HCl as raw materials [39,40], Na^+ from Na_2WO_4 and Cl^- from HCl may play similar role to NaCl. Besides, the Na^+ could insert into the hexagonal channel to stabilize the hexagonal structure [41,42]. Therefore, the addition of NaCl could facilitate the formation of h-WO_3 nuclei and their steady growth during the reaction, thus resulting in the production of h-WO_3. The o-WO_3·0.33H_2O and h-WO_3 nuclei could co-exist in the hydrothermal solution by adding a certain amount of NaCl (0.1 or 0.2 g). In addition, the hydrogen bond in the solution can induce the self-assembly of the primary self-aggregates, while van der Waals forces are favorable for enhancing the stability of the formed superstructures (such as the sunflower-like hierarchical structure) [39].

Thereby, the h-WO_3 nuclei with NaCl around them prefer to gather together, while the o-WO_3·0.33H_2O nuclei tend to grow attached to the h-WO_3. Then sunflower-like tungsten oxide hierarchical structure with 1D o-WO_3·0.33H_2O/h-WO_3 phase junction would form.

3.2. The energy band position of the o-WO_3·0.33H_2O/h-WO_3 phase junction

To experimentally confirm the existence of the o-WO_3·0.33H_2O/h-WO_3 phase junction, the Pt and MnO_x particles were photo-deposited on WNC-2. If the phase junction was successfully fabricated in the sunflower-like tungsten oxide hierarchical structure, the photo-generated electrons would transfer from one phase to another phase and the holes transfer in the opposite direction. As a result, the Pt could selectively deposit on one phase containing more electrons and the Mn^{2+} would be photo-oxidized on another phase with more holes, when H_2PtCl_6·6H_2O or $MnSO_4$·H_2O was added in the WNC-2 suspension under irradiation. Fig. S3 is the XRD patterns and XPS spectra of WNC-2 after photo-depositing Pt or MnO_x. No obvious diffraction peaks of Pt or MnO_x are found from the XRD patterns in Fig. S3a, perhaps due to the low amount or the poor crystallinity of Pt or MnO_x. However, the peak of Pt 4f (Fig. S3b) or Mn 2p (Fig. S3c) can be observed from the XPS spectra, suggesting that Pt or MnO_x was successfully deposited on the WNC-2. Meanwhile, the SEM images were also taken after photo-depositing Pt or MnO_x as presented in Fig. S4. Fig.S4a and d shows that photo-depositing Pt or MnO_x did not change the morphology of WNC-2. The nanowires in the center show similar morphology to those before depositing Pt (Fig. S4b), while some nanoparticles can be observed on the nanorods after depositing Pt (Fig. S4c). As for the sample after depositing MnO_x, it is a little difficult from Fig. S4e to distinguish whether there is MnO_x on the nanowires, possibly due to the small size of MnO_x nanoparticles. But Fig. S4f shows that the nanorods are smooth, suggesting that they may be free of MnO_x. For better confirming whether the Pt or MnO_x has been loaded on the h-WO_3 nanowires or o-WO_3·0.33H_2O nanorods, the typical TEM images, energy dispersive spectrometer (EDS) analysis, bright-field scanning transmission electron microscopy (BF-STEM), and electron energy loss spectroscopy (EELS) chemical mapping of the nanorod and nanowire in WNC-2 after photo-depositing Pt or MnO_x were presented in Figs. 6 and S5 . The typical TEM images (Fig. S5a
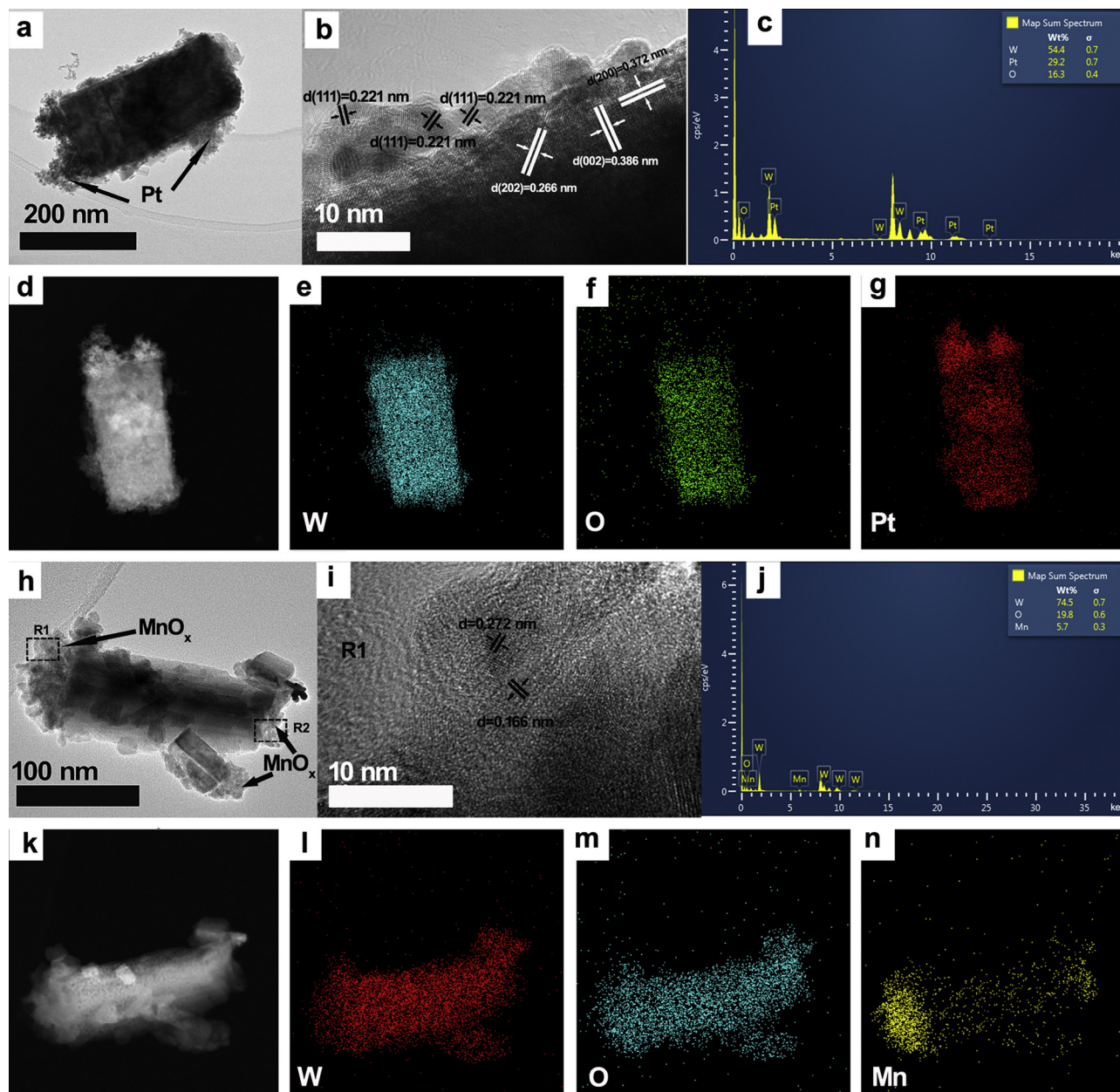
Fig. 6. The typical TEM images, EDS analysis, BF-STEM and EELS chemical mapping of WNC-2 after photo-depositing (a–g) Pt on the o-WO$_3$·0.33H$_2$O nanorod or (h–n) MnO$_x$ on the h-WO$_3$ nanowire. (The TEM samples were prepared by sonicating for about 20 min for better observing the nanorods and nanowires.).

and b) show that no Pt particles were found on the surface of the h-WO$_3$ nanowire. However, many Pt particles were found on the surface of the o-WO$_3$·0.33H$_2$O nanorod, as shown in Fig. 6a and b. It can be further confirmed by EDS analysis and EELS chemical mapping results, as shown in Fig. 6c–g. On the other hand, sponge-like manganese oxide deposits were formed on the h-WO$_3$ nanowire (Figs. 6h and i and S5c and d). HRTEM images in Figs. 6i and S5d show that the planar spaces of 0.272 and 0.166 nm well match the (222) and (440) planes of cubic Mn$_2$O$_3$, and the planar space of 0.166 nm is in accordance with the (102) plane of hexagonal MnO$_2$, suggesting the formation of MnO$_x$. The EDS analysis and EELS chemical mapping results (Fig. 6j–n) further confirm the formation of MnO$_x$ on the h-WO$_3$ nanowire. However, no sponge-like manganese oxide particles were found on the thick o-WO$_3$·0.33H$_2$O nanorod, as shown in Fig. S5e and f. The Pt and MnO$_x$ photo-deposition experiments further prove the existence of phase junction in the WNC-2 and the photo-generated electrons

transfer from h-WO$_3$ nanowire to o-WO$_3$·0.33H$_2$O nanorod and the holes move in the opposite direction.

To more deeply study the energy band position of the vertical phase junction, UV–vis absorption spectra, Mott-Schottky plots and XPS valence band spectra were studied. Fig. 7a shows that the light absorption both in the UV light and visible light region are enhanced as the amount of NaCl increases and the different absorption edges indicate the different band gaps of the samples. The inset in Fig. 7a gives the band gaps of the pure o-WO$_3$·0.33H$_2$O (WNC-1, 2.74 eV) and pure h-WO$_3$ (WNC-4, 2.85 eV). The conduction band minimum position (E$_{CBM}$) for o-WO$_3$·0.33H$_2$O and h-WO$_3$ can be estimated by the Mott-Schottky plots. As shown in Fig. 7b, the flat band potential (E$_{fb}$) for o-WO$_3$·0.33H$_2$O and h-WO$_3$ were −0.18 and −0.31 V vs. SCE (pH = 7), respectively. For n-type semiconductors, the E$_{CBM}$ is 0.1–0.3 V higher than that of E$_{fb}$ (take 0.2 V in this paper) [43]. Therefore, the E$_{CBM}$ of o-WO$_3$·0.33H$_2$O and h-WO$_3$ at
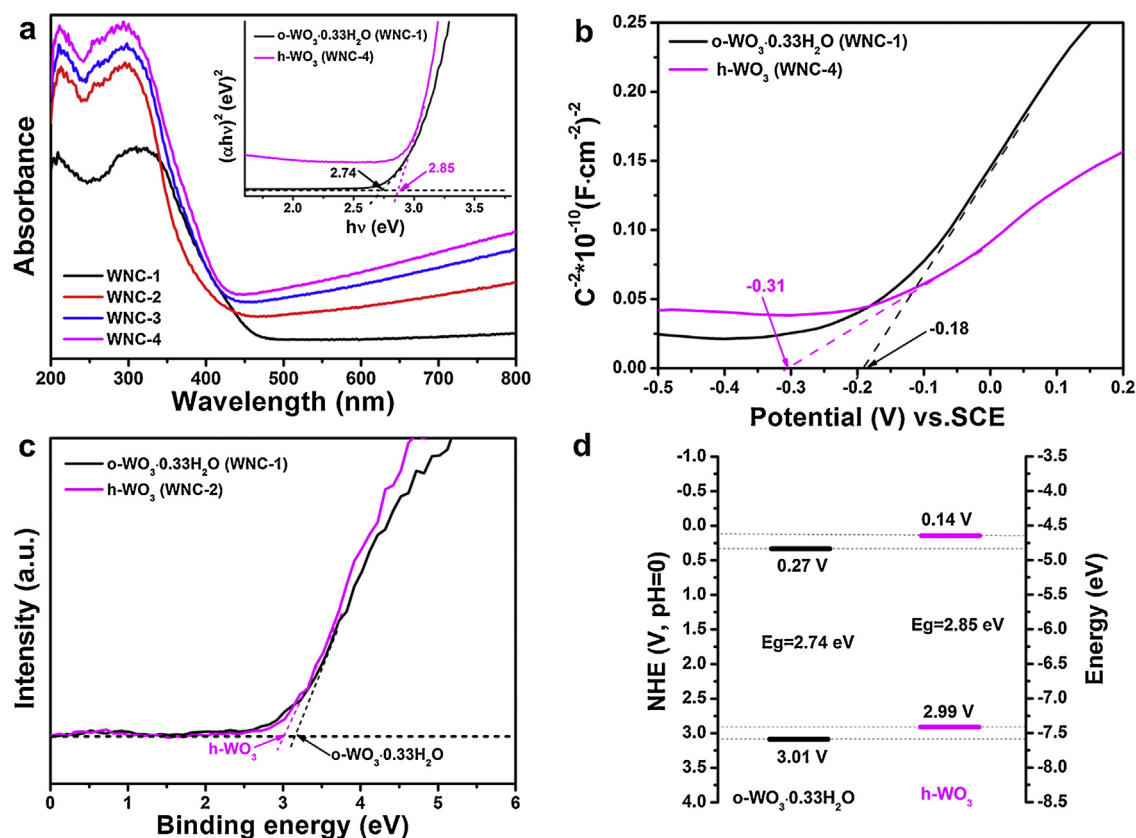
Fig. 7. (a) UV–vis absorption spectra, the plot of $(\alpha h\nu)^2$ vs $h\nu$ (the inset); (b) Mott-Schottky plots; (c) XPS valence band spectra and (d) band-edge positions of o-WO$_3$·0.33H$_2$O and h-WO$_3$.

normal hydrogen electrode (NHE, pH = 0) can be calculated using the following equation:

$$E_{CBM}(NHE, pH = 0) = E_{fb}(SCE, pH = 7) + 0.24 + 0.0591 * pH - 0.2$$

The results reveal that the E_{CBM} of o-WO$_3$·0.33H$_2$O and h-WO$_3$ were about +0.27 and +0.14 V vs. NHE, respectively. Considering the band gaps (2.74 and 2.85 eV), the valence band maximum position (E_{VBM}) of o-WO$_3$·0.33H$_2$O and h-WO$_3$ were estimated to be +3.01 and +2.99 V vs. NHE, respectively. The schematic diagram of energy level of o-WO$_3$·0.33H$_2$O and h-WO$_3$ was summarized in Fig. 7d. The E_{CBM}/E_{VBM} of o-WO$_3$·0.33H$_2$O and h-WO$_3$ were evaluated to be +0.27/+3.01 V and +0.14/+2.99 V, respectively. It was clear that the VBM of o-WO$_3$·0.33H$_2$O was lower than that of h-WO$_3$. This result could be further confirmed by XPS valence band spectra, as shown in Fig. 7c. From the analysis above, it was known that the CBM of o-WO$_3$·0.33H$_2$O were lower than h-WO$_3$, while the VBM was deeper than that of h-WO$_3$. The relative energy band position of the two phases causes the photo-generated electrons transfer from h-WO$_3$ nanowire to o-WO$_3$·0.33H$_2$O nanorod and the holes movement in the opposite direction. As a result, Pt and MnO$_x$ were selectively photo-deposited on o-WO$_3$·0.33H$_2$O and h-WO$_3$, respectively.

3.3. Photocatalytic properties

Photocatalytic experiments were conducted to evaluate the photocatalytic activities of the tungsten oxides. Fig. 8a and c shows the photodegradation of RhB and MO by the tungsten oxides. The corresponding rate constants (k), which were calculated from the pseudo-first-order linear fitting results of Fig. S6a and b, and the rate constants per specific surface area (k/S$_{BET}$) were also presented in Fig. 8b and d. Fig. 8a shows that only 62% and 52% RhB can be degraded by pure o-WO$_3$·0.33H$_2$O (WNC-1) and

pure h-WO$_3$ (WNC-4), while WNC-2 and WNC-3 with vertical o-WO$_3$·0.33H$_2$O/h-WO$_3$ phase junction could degrade 92% and 81% RhB. WNC-2 performs best in degrading RhB with the k of 2.5 and 2.8 times and the k/S$_{BET}$ of 2.6 and 4.3 times as high as those of WNC-1 and WNC-4, respectively. Similarly, as for photodegrading MO, WNC-2 and WNC-3 perform better than WNC-1 and WNC-4, as shown in Fig. 8c and d. The WNC-2 has the most excellent performance in degrading MO, with the k of 2.7 and 11.4 times and the k/S$_{BET}$ of 2.8 and 17.3 times as high as those of WNC-1 and WNC-4, respectively.

To eliminate the effect of dye self-sensitization on the photocatalytic activity, colorless phenol was further adopted as the pollutant target. Fig. 9 shows the photo-degradation activities and the corresponding rate constants k and k/S$_{BET}$. WNC-2 and WNC-3 can photodegrade 52% and 44% phenol (10 mg/L), respectively. While only 38% and 17% phenol can be degraded by pure o-WO$_3$·0.33H$_2$O (WNC-1) and pure h-WO$_3$ (WNC-4), respectively, as shown in Fig. 9a. Both the k and k/S$_{BET}$ of WNC-2 are highest among the four samples, as shown in Fig. 9b. In addition to dyes, the photodegradation of phenol confirms the superior photocatalytic performance of WNC-2 and WNC-3. To sum up, as for photodegrading dyes or phenol, the phase-junction samples perform better than the pure phases and the sample with more o-WO$_3$·0.33H$_2$O in the phase junction (WNC-2) shows higher photocatalytic performance than the sample with less o-WO$_3$·0.33H$_2$O (WNC-3).

The stability of photocatalyst was also studied. Fig. 10 shows that WNC-2 has a good recyclability in degrading RhB with only a small decline of activity after four cycles. The crystal structure of WNC-2 was unchanged after phtotocatalysis test, as shown in Fig. S7. Moreover, WNC-2 can maintain the appearance of sunflower-like structure, and the nanowires and nanorods keep their original
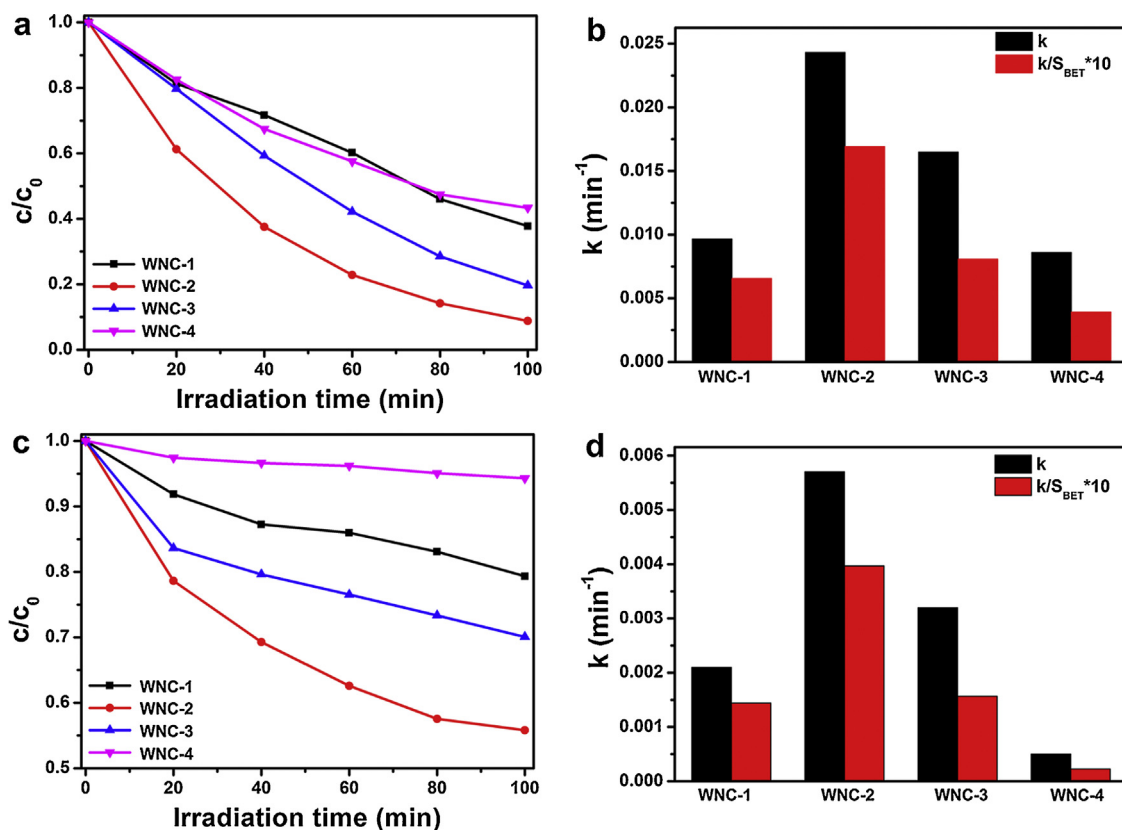
Fig. 8. Photocatalytic degradation of (a and b) RhB and (c and d) MO in aqueous solution under simulated solar light irradiation in the presence of the various tungsten oxides (k: the rate constants, calculated from the pseudo-first-order linear fitting results of Fig. S6a or b, k/S_{BET}: divided the rate constant by the specific surface area (Table S1)).
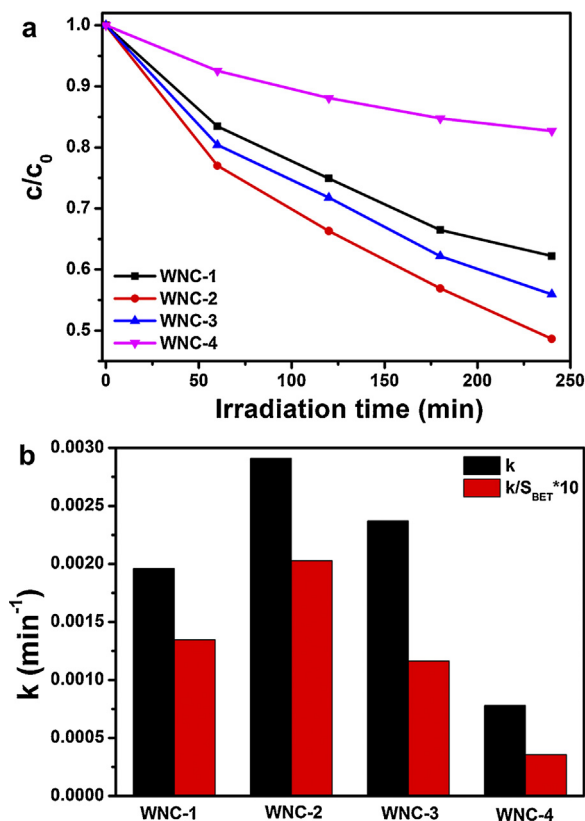
Fig. 9. (a) Photocatalytic degradation of phenol in aqueous solution under simulated solar light irradiation in the presence of the various tungsten oxides and (b) the corresponding column diagram of k and k/S_{BET}.
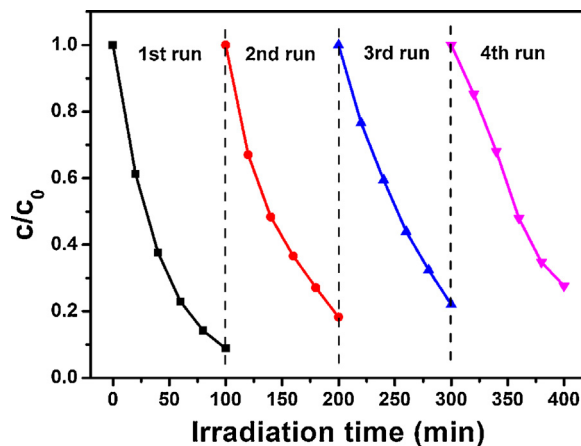
Fig. 10. The recyclability of the vertical o-WO_3·0.33H_2O/h-WO_3 phase junction (WNC-2).

structures after photocatalysis (Fig. S8). These all suggest that the as-prepared photocatalysts have good structure stability.

Since the specific surface areas of WNC-1, WNC-2, WNC-3 and WNC-4 (Table S1) show an increasing trend, while the plots of k/S_{BET} show similar variation to those of k (Figs. 8b and d and 9b), the specific surface area should not be the main factor for the variation of photocatalytic performance. The results of photodegrading RhB, MO and phenol all show that the samples WNC-2 and WNC-3 with vertical o-WO_3·0.33H_2O/h-WO_3 phase junction show better perfomance than the pure phases. It is believed that the synergetic effect between the two phases is the key factor that influences the photocatalytic performance. Moreover, the sample (WNC-2) with less h-WO_3 in the phase-junction tungsten oxide shows better
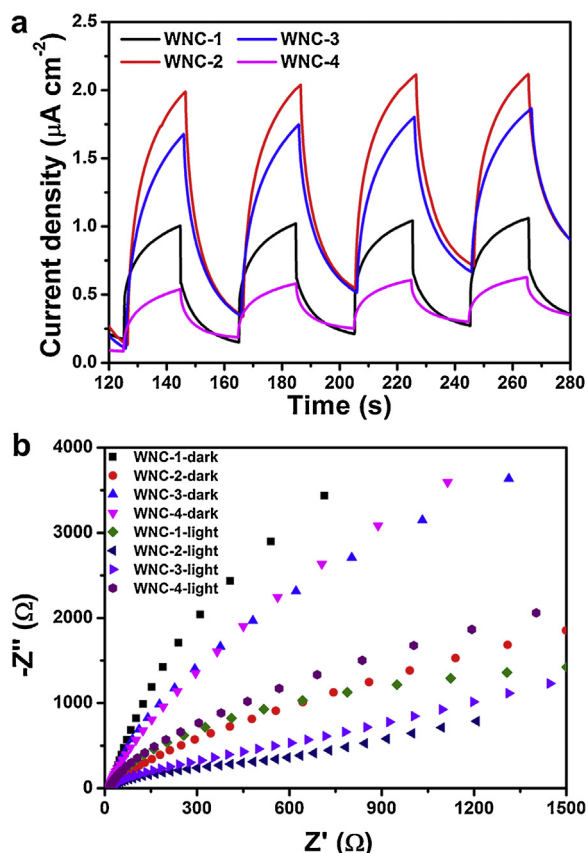
Fig. 11. (a) Photocurrent responses and (b) Nyquist plots of the samples.

photocatalytic property than the sample (WNC-3) which contains more h-WO$_3$, implying that a lower proportion of h-WO$_3$ in the phase-junction tungsten oxide is favourable for strengthening its photocatalytic capability. In summary, the construction of vertical 1D o-WO$_3$·0.33H$_2$O/h-WO$_3$ phase junction, especially the phase junction with more o-WO$_3$·0.33H$_2$O, in the tungsten oxides could significantly improve the photocatalytic performance.

3.4. The mechanism for the enhanced photocatalytic performance

The separation and transfer efficiency of photogenerated electrons and holes has a significant influence on the photocatalytic performance [44]. The photoelectrochemical performances of the samples were studied using photocurrent-time curves and the electrochemical impedance spectra (EIS). Fig. 11a shows that WNC-2 and WNC-3 with vertical o-WO$_3$·0.33H$_2$O/h-WO$_3$ phase junction have higher photocurrent density than the pure o-WO$_3$·0.33H$_2$O (WNC-1) and h-WO$_3$ (WNC-4), suggesting that the phase junction can promote the quick separation and transfer of the photogenerated charges. Moreover, the WNC-2 with a lower proportion of h-WO$_3$ in the phase-junction tungsten oxide shows higher photocurrent density than that of WNC-3. The variation of the photocurrent agrees well with that of the photocatalytic performance. The EIS were measured both in the dark and under simulated solar light irradiation, as shown in Fig. 11b. The arc radius on the EIS spectra reflects the solid state interface layered resistance and the surface charges transfer resistance. WNC-2 and WNC-3 with o-WO$_3$·0.33H$_2$O/h-WO$_3$ phase junction exhibit smaller arc radii than the pure o-WO$_3$·0.33H$_2$O (WNC-1) and h-WO$_3$ (WNC-4), also confirming the faster transfer of photogenerated charges. Both in the dark and under simulated solar light irradiation, WNC-2 has the smallest arc radii, suggesting that the reaction rate on this electrode

surface is the maximum and the electrode resistance is the smallest, so the separation and transfer of photogenerated electrons and holes in WNC-2 is the fastest. To further demonstrate the efficient separation of photogenerated electrons and holes over the phase junction, PL spectra were measured as shown in Fig. S9. The four samples all show the main PL peak at about 445 nm, which is related to the recombination of photogenerated electrons and holes [45]. Both WNC-2 and WNC-3 show a weaker PL signal than the pure phases, suggesting that the phase junction could reduce the recombination rate of the photogenerated electrons and holes. Especially, WNC-2 has a lower PL signal than WNC-3, once again proving a lower recombination rate of photo-generated electrons and holes in the sample with lower amount of h-WO$_3$. In summary, the vertical o-WO$_3$·0.33H$_2$O/h-WO$_3$ phase junction, especially the phase junction with a lower proportion of h-WO$_3$, would lead to a high separation efficiency of photogenerated carriers, thus resulting in the high efficiency of photodegrading RhB, MO and phenol.

In order to further study the photodegradation mechanism, the trapping experiments using t-BuOH (•OH scavenger) [44], EDTA-2Na (hole scavenger) [44] and p-benzoquinone (•O$_2$− scavenger) [46] were carried out, as shown in Fig. 12a and b. The process of photodegrading RhB over WNC-2 could be impeded by adding EDTA-2Na and t-BuOH, and the addition of p-benzoquinone can cause a bigger decrease on the photocatalytic performance, as shown in Fig. 12a. But neither of them greatly reduces the photocatalytic performance. This suggests that •O$_2$−, holes and •OH are all contributed to the process of photodegrading RhB. Similarly, the performance of photodegrading MO over the same sample decreases obviously after adding p-benzoquinone (Fig. 12b). The addition of EDTA-2Na and t-BuOH can also cause distinct but more moderate decline of the performance. This demonstrates that •O$_2$−, holes and •OH are all involved in the process of photodegrading MO. It seems that the conduction band edges of the as-prepared samples (Fig. 7d) are not feasible to produce •O$_2$−. However, some researchers also reported the generation of •O$_2$− by the photocatalysts with similar conduction band edge, and in some cases, •O$_2$− can be the main reactive species [46,47]. Since the band gap of WO$_3$ is about 2.8 eV, under λ£443 nm light irradiation, some electrons can be excited to be more negative potentials than the CBM to react with oxygen to generate superoxide radicals [47]. Moreover, tungsten oxide with rich defects ensures the chemisorption of molecular oxygen to the surface favoring the production of •O$_2$− [48]. Furthermore, it was found that the tungsten oxide with different morphology had different main reactive species and •O$_2$− was the main reactive species for the nanorods [49]. To confirm the results of the trapping experiments, ESR was used to detect the •O$_2$− and •OH, as shown in Fig. 12c and d. The characteristic four peaks of •OH adducts with intensity 1:2:2:1 and the six characteristic peaks of the •O$_2$− adducts clearly suggest the generation of •OH and •O$_2$− radicals.

Based on the discussion above, the schemes of the sunflower-like tungsten oxide, the structure of the vertical phase junction and the corresponding charges separation and transfer are proposed in Fig. 13. Upon irradiation of the sunflower-like tungsten oxide hierarchical structure (Fig. 13I) containing vertical o-WO$_3$·0.33H$_2$O nanorods/h-WO$_3$ nanowires phase junction (Fig. 13II), the photogenerated electrons tend to transfer from the h-WO$_3$ nanowires to the o-WO$_3$·0.33H$_2$O nanorods, while the photogenerated holes transfer from the o-WO$_3$·0.33H$_2$O nanorods to the h-WO$_3$ nanowires, driven by the potential difference caused by the different band levels of o-WO$_3$·0.33H$_2$O and h-WO$_3$ (Fig. 13III). Thus, the photogenerated electrons and holes can be spatially separated into two different phases and thus charge recombination is drastically inhibited and both the separated electrons and holes can contact the pollutants to play their roles, which greatly benefit the photocatalytic reaction. In addition, from the TEM images, the two phases
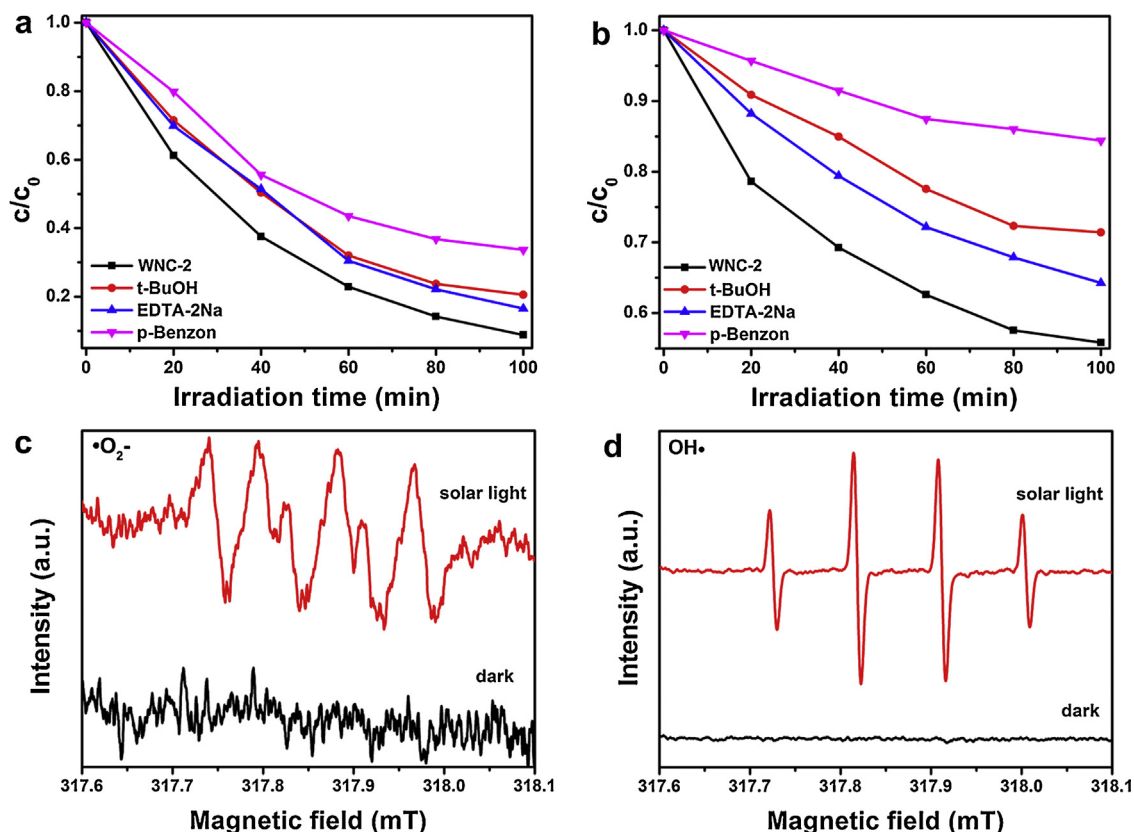
Fig. 12. The plots of photogenerated charges trapping in the system of photodegradation of (a) RhB or (b) MO over WNC-2 under simulated solar light irradiation; ESR signals of (c) the $^{\bullet}O_2-$ in the methanol and (b) the $^{\bullet}OH$ in the aqueous dispersion under simulated solar light at room temperature.
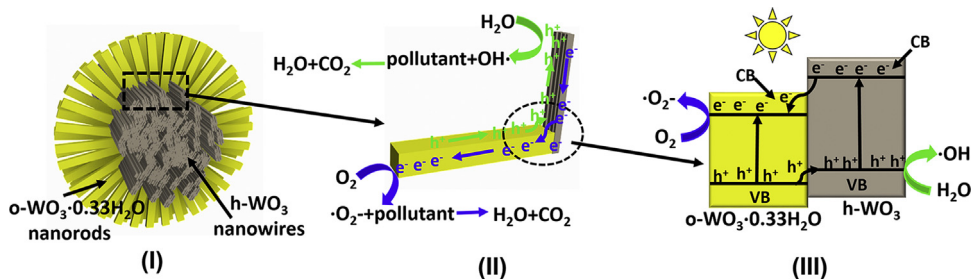
Fig. 13. The illustration of (I) sunflower-like tungsten oxide hierarchical structure, (II) the phase junction constructed by the vertical intersected o-WO$_3$·0.33H$_2$O nanorods and h-WO$_3$ nanowires and (III) the energy band position of the phase junction (CB: conduction band, VB: valence band, the charges separation and transfer are also illustrated in the (II and III)).

are both single crystals. The much lower defects in comparison with multi-crystals favour the transport of the charge carriers [20,50].

4. Conclusion

The sunflower-like tungsten oxide hierarchical structures were synthesized via a one-step hydrothermal method by adjusting the amount of NaCl. It is found that the sunflower-like tungsten oxide hierarchical structures are assembled with o-WO$_3$·0.33H$_2$O nanorods in the outer region and h-WO$_3$ nanowires in the centre region. The nanorods and nanowires substantially perpendicularly intersect at the endpoint. The XRD patterns, Raman spectra, SEM images, HRTEM images and Pt and MnO$_x$ loading experiments suggest that the vertical o-WO$_3$·0.33H$_2$O nanorods/h-WO$_3$ nanowires phase junctions are successfully constructed in this structure. The energy band position of the samples were also carefully studied and the results show that the CBM of o-WO$_3$·0.33H$_2$O were lower than

h-WO$_3$ and the VBM was deeper than h-WO$_3$, suggesting that the electrons transfer from h-WO$_3$ to o-WO$_3$·0.33H$_2$O and the holes move in the opposite direction under light irradiation. The photocatalytic performance can be greatly enhanced by the vertical phase junction and the sample with lower amount of h-WO$_3$ in the phase-junction tungsten oxide shows excellent photocatalytic properties. The results of photoelectrochemical performances show that the vertical o-WO$_3$·0.33H$_2$O/h-WO$_3$ phase junction would significantly increase the separation efficiency of photogenerated charges.

Tsinghua University (No. KF201602) and the Beijing Key Discipline Foundation of Condensed Matter Physics.

Appendix A. Supplementary data

Supplementary data associated with this article can be found, in the online version, at http://dx.doi.org/10.1016/j.apcatb.2017.02.026.

SEM images of WNC-1 and WNC-4; Lower magnification TEM images of WNC-2 and WNC-3; XRD patterns, XPS spectra, SEM images and TEM images of WCN-2 after photo-depositing Pt particles and after photo-depositing MnOx particles; pseudo-first-order linear fitting results; specific surface areas of the samples; XRD patterns, SEM images and TEM images of WCN-2 after photocatalysis; room temperature PL spectra.

References

[1] S. Wang, X. Wang, Angew. Chem. Int. Ed. 55 (2016) 2308–2320.
[2] F. Cao, J. Xiong, F. Wu, Q. Liu, Z. Shi, Y. Yu, X. Wang, L. Li, ACS Appl. Mater. Interfaces 8 (2016) 12239–12245.
[3] S. Wang, X. Wang, Small 11 (2015) 3097–3112.
[4] R. Kuriki, K. Sekizawa, O. Ishitani, K. Maeda, Angew. Chem. Int. Ed. 54 (2015) 2406–2409.
[5] S. Wang, Z. Ding, X. Wang, Chem. Commun. 51 (2015) 1517–1519.
[6] Y. Lu, G. Liu, J. Zhang, Z. Feng, C. Li, Z. Li, Chin. J. Catal. 37 (2016) 349–358.
[7] S. Wang, W. Yao, J. Lin, Z. Ding, X. Wang, Angew. Chem. Int. Ed. 53 (2014) 1034–1038.
[8] S. Wang, X. Wang, Appl. Catal. B Environ. 162 (2015) 494–500.
[9] Y. Ma, X. Wang, C. Li, Chin. J. Catal. 36 (2015) 1519–1527.
[10] Y. Zhu, Y. Liu, Y. Lv, Q. Ling, D. Liu, Y. Zhu, J. Mater. Chem. A 2 (2014) 13041–13048.
[11] Z. Huang, Q. Sun, K. Lv, Z. Zhang, M. Li, B. Li, Appl. Catal. B Environ. 164 (2015) 420–427.
[12] K. Maeda, K. Ishimaki, Y. Tokunaga, D. Lu, M. Eguchi, Angew. Chem. Int. Ed. 55 (2016) 8309–8313.
[13] A. Li, Z. Wang, H. Yin, S. Wang, P. Yan, B. Huang, X. Wang, R. Li, X. Zong, H. Han, C. Li, Chem. Sci. 7 (2016) 6076–6082.
[14] W. Wang, J. Chen, X. Zhang, Y. Huang, W. Li, H. Yu, Sci. Rep. UK 6 (2016) 20491.
[15] W. Wang, J. Chen, M. Gao, Y. Huang, X. Zhang, H. Yu, Appl. Catal. B Environ. 195 (2016) 69–76.
[16] S. Zhu, S. Xie, Z. Liu, J. Am. Chem. Soc. 137 (2015) 11532–11539.
[17] L. Pan, H. Huang, C. Lim, Q. Hong, M. Tse, O. Tan, RSC Adv. 3 (2013) 3566–3571.
[18] B. Liu, A. Khare, E.S. Aydil, ACS Appl. Mater. Interfaces 3 (2011) 4444–4450.
[19] G. Liu, X. Yan, Z. Chen, X. Wang, L. Wang, G.Q. Lu, H. Cheng, J. Mater. Chem. 19 (2009) 6590–6596.
[20] W. Li, C. Liu, Y. Zhou, Y. Bai, X. Feng, Z. Yang, L. Lu, X. Lu, K. Chan, J. Phys. Chem. C 112 (2008) 20539–20545.
[21] S. Jin, X. Wang, X. Wang, M. Ju, S. Shen, W. Liang, Y. Zhao, Z. Feng, H.Y. Playford, R.I. Walton, C. Li, J. Phys. Chem. C 119 (2015) 18221–18228.
[22] J. Liu, G. Zhang, Mater. Res. Bull. 68 (2015) 254–259.
[23] M. Ju, X. Wang, W. Liang, Y. Zhao, C. Li, J. Mater. Chem. A 2 (2014) 17005–17014.
[24] L. Shi, J. Zhang, S. Wu, Y. Li, L. Jiang, Q. Cui, J. Am. Ceram. Soc. 97 (2014) 2607–2614.
[25] X. Wang, Q. Xu, M. Li, S. Shen, X. Wang, Y. Wang, Z. Feng, J. Shi, H. Han, C. Li, Angew. Chem. Int. Ed. 51 (2012) 13089–13092.
[26] Y. Kong, H. Sun, X. Zhao, B. Gao, W. Fan, Appl. Catal. A Gen. 505 (2015) 447–455.
[27] X. Chen, Y. Zhou, Q. Liu, Z. Li, J. Liu, Z. Zou, ACS Appl. Mater. Interfaces 4 (2012) 3372–3377.
[28] P. Yang, J. Zhao, J. Wang, B. Cao, L. Li, Z. Zhu, J. Mater. Chem. A 3 (2015) 8256–8259.
[29] Y. Liu, Q. Li, S. Gao, J.K. Shang, CrystEngComm 16 (2014) 7493–7501.
[30] J. Cao, B. Luo, H. Lin, B. Xu, S. Chen, Appl. Catal. B Environ. 111 (2012) 288–296.
[31] F.X. Xiao, J.W. Miao, H.B. Tao, S.F. Hung, H.Y. Wang, H.B. Yang, J.Z. Chen, R. Chen, B. Liu, Small 11 (2015) 2115–2131.
[32] K. Li, M. Han, R. Chen, S. Li, S. Xie, C. Mao, X. Bu, X. Cao, L. Dong, P. Feng, Y. Lan, Adv. Mater. 3 (2016) 1–6.
[33] S. Khanchandani, S. Kundu, A. Patra, A.K. Ganguli, J. Phys. Chem. C 117 (2013) 5558–5567.
[34] S. Liu, N. Zhang, Z. Tang, Y. Xu, ACS Appl. Mater. Interfaces 4 (2012) 6378–6385.
[35] Y. Li, Z. Tang, J. Zhang, Z. Zhang, CrystEngComm 17 (2015) 9102–9110.
[36] C. Santato, M. Odziemkowski, M. Ulmann, J. Augustynski, J. Am. Chem. Soc. 123 (2001) 10639–10649.
[37] J. Wang, E. Khoo, P.S. Lee, J. Ma, J. Phys. Chem. C 113 (2009) 9655–9658.
[38] J. Wang, E. Khoo, P.S. Lee, J. Ma, J. Phys. Chem. C 112 (2008) 14306–14312.
[39] J. Yin, H. Cao, J. Zhang, M. Qu, Z. Zhou, Cryst. Growth Des. 13 (2013) 759–769.
[40] Q.H. Li, L.M. Wang, D.Q. Chu, X.Z. Yang, Z.Y. Zhang, Ceram. Int. 40 (2014) 4969–4973.
[41] A. Phuruangrat, D.J. Ham, S.J. Hong, S. Thongtem, J.S. Lee, J. Mater. Chem. 20 (2010) 1683–1690.
[42] L. Chen, S. Lam, Q. Zeng, R. Amal, A. Yu, J. Phys. Chem. C 116 (2012) 11722–11727.
[43] Z. Zhao, T. Butburee, M. Lyv, P. Peerakiatkhajohn, S. Wang, L. Wang, H. Zheng, RSC Adv. 6 (2016) 68204–68210.
[44] Y. Lv, Y. Liu, Y. Zhu, Y. Zhu, J. Mater. Chem. A 2 (2014) 1174–1182.
[45] J. Sun, J. Guo, J. Ye, B. Song, K. Zhang, S. Bai, R. Luo, D. Li, A. Chen, J. Alloy Compd. 692 (2017) 876–884.
[46] J. Wang, W. Shi, D. Liu, Z. Zhang, Y. Zhu, D. Wang, Appl. Catal. B Environ. 202 (2017) 289–297.
[47] X. Xiao, R. Hu, S. Tu, C. Zheng, H. Zhong, X. Zuo, J. Nan, RSC Adv. 5 (2015) 38373–38381.
[48] N. Zhang, X. Li, H. Ye, S. Chen, H. Ju, D. Liu, Y. Lin, W. Ye, C. Wang, Q. Xu, J. Zhu, L. Song, J. Jiang, Y. Xiong, J. Am. Chem. Soc. 138 (2016) 8928–8935.
[49] M. Farhadian, P. Sangpour, G. Hosseinzadeh, J. Energy Chem. 24 (2015) 171–177.
[50] G. Tian, H. Fu, L. Jing, B. Xin, K. Pan, J. Phys. Chem. C 112 (2008) 3083–3089.